Journal of Neuroinflammation

RESEARCH

Open Access

Dorsoventral photobiomodulation therapy safely reduces inflammation and sensorimotor deficits in a mouse model of multiple sclerosis

Vincent Escarrat[1,2,5], Davide Reato[1,3], Guillaume Blivet[5], Jacques Touchon[4], Geneviève Rougon[1], Rémi Bos[1*†] and Franck Debarbieux[1,2,6*†]

Abstract

Background Non-invasive photobiomodulation therapy (PBMT), employing specific infrared light wavelengths to stimulate biological tissues, has recently gained attention for its application to treat neurological disorders. Here, we aimed to uncover the cellular targets of PBMT and assess its potential as a therapeutic intervention for multiple sclerosis (MS).

Methods We applied daily dorsoventral PBMT in an experimental autoimmune encephalomyelitis (EAE) mouse model, which recapitulates key features of MS, and revealed a strong positive impact of PBMT on the sensorimotor deficits. To understand the cellular mechanisms underlying these striking effects, we used state-of-the-art tools and methods ranging from two-photon longitudinal imaging of triple fluorescent reporter mice to histological investigations and patch-clamp electrophysiological recordings.

Results We found that PBMT induced anti-inflammatory and neuroprotective effects in the dorsal spinal cord. PBMT prevented peripheral immune cell infiltration, glial reactivity, as well as the EAE-induced hyperexcitability of spinal interneurons, both in dorsal and ventral areas, which likely underlies the behavioral effects of the treatment. Thus, aside from confirming the safety of PBMT in healthy mice, our preclinical investigation suggests that PBMT exerts a systemic and beneficial effect on the physiopathology of EAE, primarily resulting in the modulation of the inflammatory processes.

Conclusion PBMT may therefore represent a new valuable therapeutic option to treat MS symptoms.

Keywords Photobiomodulation therapy, Experimental autoimmune encephalomyelitis, Inflammation, Neuroprotection

†Rémi Bos and Franck Debarbieux contributed equally.

*Correspondence:
Rémi Bos
remi.bos@univ-amu.fr
Franck Debarbieux
franck.debarbieux@univ-amu.fr
[1] Aix Marseille Univ, CNRS, INT, Inst. Neurosci. Timone, Marseille, France
[2] Aix Marseille Univ, CNRS, CERIMED, Marseille, France
[3] Département BEL, Mines Saint-Etienne, Centre CMP, 13541 Gardanne, France
[4] University of Montpellier, Montpellier, France
[5] REGEnLIFE, Paris, France
[6] Institut Universitaire de France (IUF), Paris, France

Introduction

In recent years, non-invasive photobiomodulation (PBM), employing specific red and near-infrared light wavelengths, has gained attention for its therapeutic potential in tretating multiple diseases with no serious adverse effects reported [1, 2], rendering it a valuable option to treat neural-related diseases [3–5]. In animal models, PBM therapy (PBMT) has been effective in managing locomotor disabilities associated with Parkinson's disease [6, 7], motor disorders related to multiple sclerosis (MS) [8–10], and cognitive disorders in Alzheimer's disease [11, 12]. Early results from ongoing clinical trials also indicate potential benefits of PBMT for treating Alzheimer's disease patients [13] and multiple sclerosis (MS) patients [14].

Whereas PBMT triggers photochemical changes within cellular structures, the mechanisms underlying its beneficial effect at a systemic level are not fully understood. The most widely accepted mechanism of action is that PBMT improves cellular functions via a direct effect on mitochondrial activity, involving a chromophore, the cytochrome *c* oxidase [15–18]. Several reports have documented how this photobiomodulation of mitochondrial activity can facilitate neuronal recovery in neurodegenerative diseases [19].

MS is a severe autoimmune disorder that affects more than 2.8 million people worldwide. MS patients suffer from the related progressive lifelong locomotor and cognitive disabilities that impede their quality of life [20]. The clinical course of MS falls into two main subtypes. Relapsing–remitting MS diagnosed in > 85% of patients is transient and characterized by relapses of disease separated by periods without clinical signs. However, for approximately 15% of people, MS is progressive, with irreversible neurological deterioration occurring either from the disease onset (primary progressive) or after a prolonged relapsing–remitting period (secondary progressive). It is now recognized that progression occurs throughout the disease course, independent of relapse activity, a phenomenon termed progression independent of relapse activity (PIRA) [21].

MS likely develops as a result of a dynamic interplay among genetic, environmental, and lifestyle factors. Despite a low incidence of familial MS (< 13%) [22], predisposing genetic factors [23, 24] can amplify the susceptibility to early-life encounters with environmental pathogens [25]. These encounters, in turn, contribute to shape adaptive immune responses, influencing the subsequent reactivity toward self-antigens in adulthood. Depending on one's acquired repertoire of pathogen-specific B and T regulatory leukocytes [25], infection by typically innocuous viruses like Epstein-Barr virus or the human herpes virus [26, 27] can turn into a detrimental triggering event. Autoreactive leukocytes could thus be reactivated through molecular mimicry between viral sequences and myelin protein, potentially leading to MS [26, 28]. While the exact cause of MS remains unknown, such a scenario is worthy of attention considering the number of worldwide viral pandemics experienced in recent years and their acknowledged relevance to MS incidence [29].

There are four key pathological features of MS: (i) inflammation, believed to be the main trigger of the cascade of events leading to tissue damage; (ii) demyelination, where the myelin sheath or the oligodendrocyte cell body is destroyed by the inflammatory process; (iii) axonal damages or losses; and (iv) reactive gliosis [20]. Complex interactions among peripheral immune cell subsets (i.e., $LysM^+$ myeloid cells), astrocytes, microglia, oligodendrocytes, and neurons play intricate roles in the control of neurotransmission, inflammation, and neurodegeneration.

Despite significant progress in identifying relevant cell subsets and targets for their specific modulation, therapeutic strategies remain limited. Pharmacological treatments specific to MS effectively alleviate symptoms but may entail adverse effects, underscoring the need for novel therapeutic modalities with more favorable safety profiles [30, 31].

The murine model of experimental autoimmune encephalomyelitis (EAE) has been instrumental in recapitulating key features of MS [32]. This model provides crucial insights into the immunological aspects of MS [33] and presents potential avenues for therapeutic interventions [20]. We induced EAE in adult triple heterozygous Thy1-ECFP//LysM-EGFP//CD11c-EYFP reporter mice [34] to follow the dynamics of axons and innate inflammatory cell subsets.

In this study, we aimed to (i) evaluate the safety and efficacy of an optimized red and near-infrared PBMT device, simultaneously targeting both the back and the abdomen, for its application on the sensorimotor deficits observed in the EAE mouse model of MS and (ii) to obtain insights into the dynamics of its effect on neuroinflammatory cellular interactions. We showed that PBMT significantly decreased inflammation and axonal losses, preventing neuronal hyperexcitability and improving sensorimotor deficits. Dorsoventral PBMT may thus represent a valuable non-invasive and safe therapy for MS.

Materials and methods

We implanted a glass window in 50 adult (> 15 weeks) triple heterozygous Thy1-ECFP//LysM-EGFP//CD11c-EYFP transgenic mice of either sex, and induced EAE in 35 of them. Seven mice did not develop clinical signs and were removed from the study. An endpoint for the

experiments was fixed when weight loss exceeded 20% of the initial body weight during three consecutive days; none had to be excluded based on this criterion.

Mice of either sex were randomized in four groups: (1) EAE-induced (EAE), (2) EAE-induced and treated by PBMT (EAE-PBMT), (3) healthy control (CTRL), and (4) healthy control treated by PBMT (CTRL-PBMT). We determined sample size to mimize the number of experimental animals involved while providing sufficient power to detect statistical differences. The numbers of animals and biological replicates are specified in each figure legend. Automated image analysis was conducted after two-photon imaging and immunohistochemistry. Operators were moreover blinded to mouse experimental conditions for all outcome measures of functional locomotor deficits and for image analyses.

Spinal cord glass window implantation

As described previously [35, 36], a glass window was cemented and sealed on the exposed spinal parenchyma. Briefly, mice were deeply anaesthetized with an intraperitoneal injection of ketamine/xylazine (120 mg/kg or 12 mg/kg) administration prior to dorsal midline incision over T12–L2 and scalpel resection of their muscles between the spinal and transverse processes. Animals were then suspended on a spinal-fork stereotaxic apparatus (Harvard Apparatus) to facilitate the fixation of the metallic scaffold later serving as an anchoring point for surgery and imaging. Once it was firmly held by its handle, spinal processes were drilled and removed to expose the dorsal spinal tissue. A line of liquid Kwik-Sil (World Precision Instruments) was applied to the dura mater surface along the midline of the spinal cord, and the glass window was immediately glued and hermetically cemented over the spinal cord. Postoperative analgesia was applied immediately following surgery and every two days for 10 days. EAE was induced three weeks after glass window implantation, at which time surgical-related inflammation had resumed.

EAE induction

Three weeks after the surgery, mice were deeply anaesthetized and subcutaneously injected with an emulsion of MOG 35–55 peptide (200 µg, GMPT1519-80, Proteogenix) and Freund's complete adjuvant. The complete adjuvant was prepared with incomplete Freund's adjuvant (F5506 Sigma-Aldrich) supplemented with 800 µg of mycobacterium tuberculosis (BD Difco #231141), as described [34]. Induction was completed by intraperitoneal (i.p.) injections of 400 ng of pertussis toxin (#3097 Torcis) in PBS the same day and two days after. As CTRL and CTRL-PBMT mice were not EAE-induced, "time post-induction" in the figures means the time after the three weeks of recovery following surgery.

Dorsoventral PBMT

We used the RGn535 noninvasive preclinical device manufactured by REGEnLIFE (Paris, France) for mouse contention and dorsoventral PBMT. The device is tailored to immobilize mice safely and securely while delivering targeted PBMT. It includes two identical PBMT modules (one dorsal and one ventral, Fig. 1C) whose positions can be adjusted to target light at the desired locations for mice of varying sizes. Positions were set symmetrically above the spinal window center and on the clean shaven belly of a vigil mouse. The shuttle was tailored to accommodate the handle of the implanted spinal chamber.

Each PBMT module was composed of three different energy sources: one near-infrared (NIR) laser diode (850 nm) and two light-emitting diodes (LEDs), respectively, at 850 nm and 660 nm. The photonic emissions were pulsed at a 10 Hz frequency through a ring-shaped magnet, creating a static magnetic field at 200 mT (Table 1).

After a short phase of habituation (< 5 days), mice autonomously entered the illuminating shuttle into the RGn535. The temperature inside the shuttle never raised more than 0.5 °C during the 6 min PBMT protocol, and illumination did not induce signs of discomfort in the mice. On D12 following EAE induction, corresponding to the day of the first clinical signs, mice were submitted to the treatment procedure for 6 min per day, with or without light illumination, to evaluate the effect of PBMT on the course of the disease.

Functional analysis of locomotor deficits

Clinical score

EAE progression was evaluated daily by assigning a clinical score as follows: 0, no detectable signs; 0.5, flaccid tail; 1, complete tail paralysis; 2, partial hind limb paralysis; 2.5, unilateral complete hind limb paralysis; 3, complete bilateral hind limb paralysis; 3.5, complete hind limb paralysis and partial forelimb paralysis; 4, total paralysis of forelimbs and hind limbs; and 5, death. The progression profile of the clinical scores throughout the 28-day protocol allowed us to divide it into four periods: baseline (D0–D11), onset (D12–D16), peak (D17–D21), and recovery (D22–D28).

Sensorimotor coordination

The rotarod test required the mouse to balance itself while running on a rod. It was performed in a ramping mode using a rotating rod (#47650 Ugo Basile SRL) that accelerated over 5 min from 5 to 40 rotations per minute

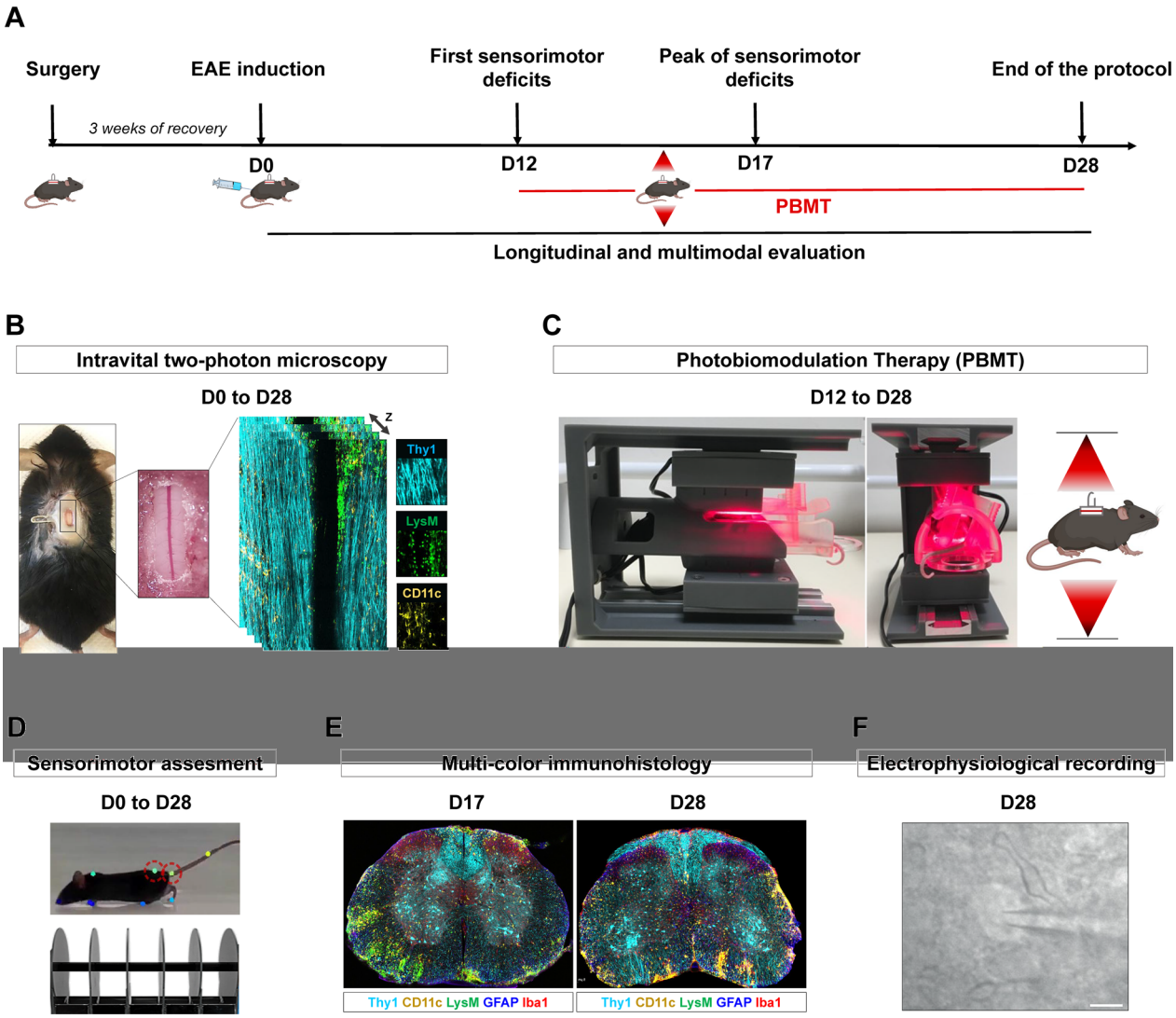

Fig. 1 Longitudinal and multimodal evaluations of photobiomodulation therapy (PBMT) from a mouse model of MS. **A**–**F** Outline of the experimental protocol. Note that the mice were divided into four groups: EAE, EAE-PBMT, CTRL, and CTRL-PBMT (**A**). Spinal cord glass window was implanted on triple transgenic fluorescent reporter mice (Thy1-ECFP//LysM-EGFP//CD11c-EYFP) for intravital imaging (**B**). Three weeks after the surgery, mice were immunized using the active EAE model of MS. From the onset of the first sensorimotor symptoms (D12) to the end of the study (D28), half of the animals were treated with PBMT consisting of a near-infrared light stimulation 6 min/day (**C**). Sensorimotor deficits were assessed with clinical EAE scoring, rotarod test, and analysis based on DeepLabCut tracking throughout the protocol (**D**). Neuroinflammation was evaluated in a longitudinal way with two-photon intravital microscopy (**B**) and histological analysis on coronal spinal slices at D17 and D28 (**E**). Finally, electrophysiological properties of two neuronal populations were recorded at D28 post-immunization (**F**)

(rpm). On each evaluation day, the latency of the mouse to fall was recorded.

Postural deficits

To precisely analyze postural deficits during spontaneous locomotion, mice were placed in a transparent cage (33 cm × 16 cm × 13 cm) for about 5 min. Short profile videos, including typically 4–5 events of spontaneous cage crossing, were acquired at 30 fps using a regular USB camera. Locomotion periods were defined using the x-position of the mouse's mouth/nose during its crossing from one side of the cage to the other. DeepLabCut [37] was used to automatically identify anatomical points of interest in the videos as well as the position of the box corners to normalize x and y positions of anatomical labels of interest. Training was achieved by manual labeling of five frames for each individual video. The output data generated with DeepLabCut was further analyzed

Table 1 Technical specifications of the preclinical RGn535 PBMT device

Component	Laser diode	IR LED	Red LED
Wavelength (nm)	850	850	660
Mode	Pulsed wave at 10 Hz; 50% duty cycle		
Power density (irradiance max.—mW/cm^2)	8.86	18.50	13.23
Dose (fluence max. for 6 min. exposure—J/cm^2)	1.59	3.33	2.38
Cumulated dose (for 17 treatments—J/cm^2)	27.03	56.61	40.46
Total number (dorsal module)	1	1	1
Total number (ventral module)	1	1	1

using custom MATLAB scripts (available source at link). Robust estimates of the positions of the labeled points were obtained from the median values across all the frames of the locomotion period present in the video. Those values were then averaged across the videos belonging to a given disease stage.

To identify locomotion periods, we used the x-position of the mouse mouth/nose to identify periods in which the animal crosses from one side of the cage to the other. To estimate the hind limb motion during locomotion, we used the standard deviation of the y-position after detrending the signal to correct for slow variations in the y-position. This step was necessary considering the small range of motion of the limbs compared with slight asymmetries in the box positioning. These asymmetries result in shifts in the y-direction when animals move from one side of the box to the other and therefore mask the true range of motion of the limbs.

We observed no significant differences in the effects of PBMT on locomotor and postural deficits between EAE mice with spinal glass window implants and those without. Consequently, we pooled the data for analysis.

Immunohistology

On D17 or D28 after EAE induction, mice were intracardially perfused with 25 ml of 1× phosphate-buffered saline (PBS) at 4 °C, followed by 4% paraformaldehyde (Electron Microscopy Science #15710) at RT. Then spinal cords were gently removed with fine Dumont forceps and scissors (FST) placed in PBS, post-fixed overnight in 4% PFA, and then stored at 4 °C in PBS (1×)/Na-azide (0.1 g/L). On the day of the immunofluorescence experiment, thoracic segments (T12–L2) of the fixed spinal cord were embedded in an agarose gel (3.5%) and cut into 50 µm-thick coronal sections using a vibratome (Leica Microsystem). Immunostaining was performed on 3–5 slices located below the glass window and interspaced at 500 µm. Freshly cut slices were then placed in a blocking buffer (1% IgG-free BSA, 10% normal donkey serum, 0.2% Triton X-100 in PBS) for 90 min prior to their incubation with primary antibodies diluted in a blocking buffer overnight at 4 °C under gentle agitation. Primary antibodies were then washed four times (5 min/washes) in PBS before a 2 h incubation in secondary antibodies diluted in a blocking buffer without Triton X-100 at room temperature. The secondary antibodies were then washed three times (5 min/washes) in PBS before mounting with aqueous medium (Fluoromount F4680). Anti-IBA1 (Wako #019-19741, 1/750) was used in combination with Alexa Fluor® 647-conjugated antibody (Jackson #711-605-152, 1/400), while anti-GFAP (Invitrogen #PA1-10004, 1/750) was used with DyLight® 405-conjugated antibody (Jackson #703-475-155, 1/400). Given the triple endogenous staining for Thy1, LysM, and CD11c, we obtained spinal cord slices shining with five fluorescent colors.

Imaging

Two-photon intravital imaging

Each mouse was longitudinally imaged before and at 7, 10, 14, 17, 21, 24, and 28 days after EAE induction. For each imaging session, mice were anesthetized with an intraperitoneal injection of ketamine/xylazine (100 mg/kg or 10 mg/kg) administration. Freely breathing animals were placed in a microscope chamber warmed to 32 °C to maintain the body temperature at 37 °C. A tunable femtosecond pulsed laser (Ultra II Chameleon Coherent) was coupled with a Zeiss two-photon (2P) microscope (LSM 780, Carl-Zeiss) equipped with a 20×water-immersion objective lens (NA = 1.0) and five non-descanned detectors. The resulting field of view was typically 424 µm×424 µm. The laser was tuned to 940 nm to optimize the simultaneous excitation of the labeling fluorophore combination. Filter sets were designed to optimize the separation of the emission spectra of multiple fluorophores (420–490 nm, 498–510 nm, 520–550 nm, 555–600 nm, 608–678 nm). For each image stack, the laser intensity was adjusted according to imaging depth in order to maximize signal intensity while minimizing saturation throughout the image stack. A second harmonic signal reflected by superficial collagen fibers was

used to identify meninges. Blood vessels and remarkable axon patterns were used as anatomical markers to find the region of interest for each animal. Tiled stacks of 2D images were acquired every 3 µm along the z-axis to generate a typical volume of interest of 2500 × 1250 × 100 μm^3 starting at the level of the meninges. Angular micro adjustments during mouse repositioning allowed the imaging of the same volume of interest throughout imaging sessions.

Confocal imaging

Immunostained slices were imaged in a confocal mode on an LSM 780 (Carl-Zeiss) using a 20 × water-immersion objective lens (NA = 1.0) with the following excitation laser lines: 405 nm, 458 nm, 488 nm, 514 nm, and 633 nm. Emitted fluorescence was collected on the tunable spectrometric Quasar detection unit using the following bands: 389–455 nm, 460–486 nm, 505–511 nm, 536–580 nm, and 655–717 nm. Tiled stacks of 2D images were acquired over a depth of 25 µm using an optical sectioning of 5 µm.

Image analysis

Images were analyzed using ZEN 2.1 (Zeiss, Jena, Germany) and Arivis Vision 4D software (Arivis AG, Berlin, Germany V3.6.2).

Intravital images

Images were spectrally unmixed, cropped, and manually registered across sessions using ZEN 2.1. The volume of interest (VOI) lying between 30 and 50 µm below the dura mater was typically used for quantitative analysis. In this volume, individual immune cells were automatically segmented and counted in the total 3D volume of the cropped images using a custom-designed pipeline on the Arivis software. The pipeline was based on the blob-finder algorithm and used different feature filters such as color, size, intensity, sphericity, and volume to separate the cells into three classes: $LysM^+$ circulating cells, $LysM^+$ infiltrated cells, and $CD11c^+$. Cell densities were evaluated per volume unit of 0.01 mm^3 to minimize VOIs' inter-animal variability. Axonal densities were evaluated on maximum intensity projections images at six different locations along the rostro-caudal axis, which were carefully repositioned across imaging sessions. Fluorescence intensity profiles of the axonal staining ($Thy1^+$) were used along 300 µm segments lying perpendicular to the dorsal vein. Each peak of fluorescence above a predetermined threshold value was counted as an axon whose location was classified according to its proximity to the dorsal vein: proximal (0–100 µm), medial (100–200 µm), and distal (200–300 µm). The average axonal density over the six locations was used for the statistical analyses.

Confocal images

Modified versions of the in vivo Arivis pipeline (V3.6.2) were used to perform object segmentation on the maximum intensity projection images of the whole spinal cord slices. The blob-finder algorithm was combined with available feature filters to classify six different cell subtypes: $Thy1^+$ axons, $Thy1^+$ somas, $LysM^+$ cells, $CD11c^+$ cells, $Iba1^+$ cells, and $GFAP^+$ processes. Cell densities were evaluated per volume unit of 0.01 mm^3 to minimize the interslice variability while offering a comparison opportunity with intravital data. Regional masks were then overlaid to characterize differences of cell density between dorsal and ventral regions of the spinal cord as well as between WM and GM. Physical contacts between $Iba1^+$ and $GFAP^+$ objects were evaluated via the intersecting compartment tool in Arivis. The number of contacts was normalized by the number of $Iba1^+$ cells to define the number of contact/cells. $LysM^+$ cell infiltrative behavior on D17 was calculated by measuring the minimum distance of each cell from the manually defined border of the spinal cord slice.

Electrophysiological study

Ex vivo preparations

Deeply anesthetized mice were decapitated prior to fast spinal cord removal by laminectomy. Fresh tissue was placed in ice-cold (1–2°) aCSF containing (in mM) 252 sucrose, 3 KCl, 1.25 KH_2PO_4, 4 $MgSO_4$, 0.2 $CaCl_2$, 26 $NaHCO_3$, 25 D-glucose, and pH 7.4, bubbled with 95% O_2 and 5% CO_2. The meninges were then removed and the spinal cord (T12–L5) embedded in a 1% agarose solution. L1–3 lumbar segments were sliced into 325 µm coronal sections using a vibrating micotome (Leica, VT1000S) and an ice-cold slicing solution (1–2°) containing (in mM) 130 K-gluconate, 15 KCl, 0.05 EGTA, 20 HEPES, 25 D-glucose, 3 kynurenic acid, and pH 7.4 with NAOH [38]. After a resting period of 30–60 min at 32–34 °C in regular aCSF containing (in mM) 120 NaCl, 3 KCl, 1.25 NaH_2PO_4, 1.3 $MgSO_4$, 1.2 $CaCl_2$, 25 $NaHCO_3$, 20 D-glucose, and pH 7.4, individual slices were transferred to the recording chamber filled and superfused with the same bubbled (95% O_2 and 5% CO_2) regular aCSF. All recordings were made with the regular aCSF at 32–34 °C.

Electrophysiology

Whole-cell patch-clamp recordings were performed using a Multiclamp 700B amplifier driven by Pclamp 10 software (Molecular Devices) either from ventromedial premotor neurons (lamina X) or from sensory dorsal horn neurons (lamina I–II). Patch electrodes (5–7 MΩ) were pulled from borosilicate glass capillaries (1.5 mm OD, 1.12 mm ID; #TW150-4; World Precision Instruments) on a Sutter P-97 puller (Sutter Instruments

Company) and filled with an intracellular solution (in mM): 140 K^+-gluconate, 5 NaCl, 2 $MgCl_2$, 10 HEPES, 0.5 EGTA, 2 ATP, 0.4 GTP, and pH 7.3. Pipette and neuronal capacitive currents were canceled, and after breakthrough, the series resistance was compensated. Recordings were digitized online and filtered at 10 kHz (Digidata 1440A, Molecular Devices). All experiments were designed to gather data within a stable period (i.e., at least 2 min after establishing whole-cell access). Because (i) the cell size influences neuronal excitability [39] and because (ii) we recorded non-identified neurons, we only compared the electrophysiological parameters of cells with the same size in both conditions to avoid any recording bias related to their morphological features.

Data analysis

Electrophysiological data was analyzed with Clampfit 10 software (Molecular Devices). Only neurons with a stable membrane potential below − 55 mV, stable access resistance (no > 20% variation), and overshooting action potentials were analyzed. Reported membrane potentials were corrected for liquid junction potentials.

We determined the input resistance by the slope of linear fits to voltage responses evoked by small positive and negative current injections. Firing properties were measured from depolarizing current pulses of varying amplitudes. The rheobase was defined as the minimum step current intensity required to induce an action potential from the membrane potential held at the resting membrane potential (Vrest). The voltage threshold for firing was determined on the first spike of the depolarizing current step at rheobase, as the point at which the first derivative of the voltage reached 10 mV/ms [40].

To determine the frequency-current (F-I) relationship, depolarizing current steps of increasing amplitude were delivered, and the spike number during the entire step duration (600 ms) was determined and plotted against the amplitude of the injected current from the rheobase. The slope of the plot was linearly fitted. The maximum instantaneous firing frequency was determined as the largest number of the inverse of the interspike interval during the most depolarized current step. The cell body cross-sectional area was automatically calculated using FIJI software.

Statistics

All statistical analysis was performed using Graph Pad Prism® 9. Values are expressed as means ± standard error of the mean (SEM). Statistical comparisons between each group were performed using the nonparametric two-tailed Mann–Whitney U test. Simple linear regression was performed to evaluate the correlation between two variables. Significance was assessed using a 95% confidence level and the degree of significance presented by *P < 0.05; **P < 0.01; ***P < 0.001; NS, not significant.

Results

PBMT alleviates sensorimotor deficits in EAE mice

To investigate the potential impact of PBMT on MS, we employed adult triple heterozygous Thy1-ECFP//LysM-EGFP//CD11c-EYFP transgenic mice [34] of either sex, and induced EAE in part of them (see "Methods") in the absence or presence of a spinal glass window to allow recurrent in vivo imaging. In the latter case, we induced EAE three weeks after the implantation of a spinal glass window to allow resorption of the inflammation induced by surgery. Whereas the window itself did not significantly impede the mice behavior over weeks, the first signs of tail paralysis were clearly observed 12–14 days after induction. The sensorimotor deficits of the EAE-control and PBMT-treated mice were meticulously assessed throughout the 28 days post-induction (Figs. 1A–C, 2). EAE clinical scoring revealed a gradual onset of sensorimotor paralysis in the hindlimbs, reaching a maximum around day 17 (D17). Subsequently, there was spontaneous, albeit modest, recovery by the end of the protocol at D28 (Fig. 2A).

We conducted identical behavioral analyses on EAE-PBM-treated mice, receiving daily PBMT (6 min, 660 nm–850 nm; see "Methods" and Table 1) starting from D12. We previously assessed an absence of functional side effects in control mice following the same treatment (Fig. S1A). A four-day consecutive PBMT period was sufficient to observe a significant deceleration in disease progression (Fig. 2A). Notably, daily PBMT demonstrated efficacy at the disease onset *($p = 0.018$)*, attenuating significantly the sensorimotor deficits at the peak *($p < 0.001$)* and the recovery phases *($p < 0.001$)*. We verified that the glass window did not modify the efficiency of PBMT treatment. Furthermore, sensorimotor symptoms were reduced by half at D28 and became residual (Fig. 2A).

In parallel to the EAE clinical scoring, we evaluated the locomotor deficits using the accelerating rotarod task on the same mice (Fig. 2B). A very significant effect of PBMT was observed at the peak *($p = 0.004$)*, and recovery *($p < 0.001$)* phases of the disease (Fig. 2B). Mice were also able to run at almost twice faster speeds on the accelerating rotarod task (Fig. 2B) as expected from the negative correlation between the locomotor performances and the EAE clinical scores (Fig. 2C).

In a subset of animals where we recorded videos over multiple days, postural deficits of EAE mice were further characterized using analyses based on DeepLabCut (DLC) tracking (Fig. 2D) considering the whole video duration (Fig. 2E, F) as well as restricting the analyses to

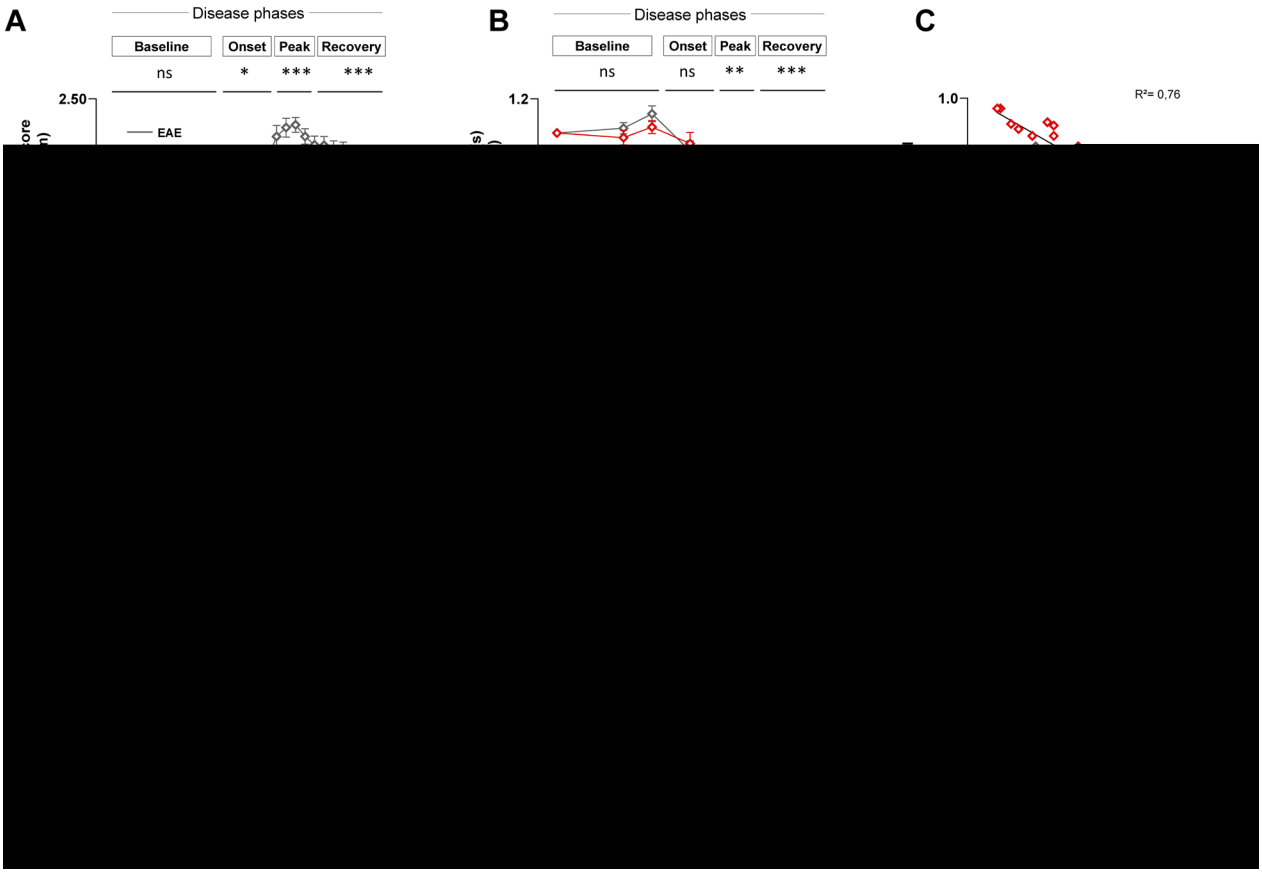

Fig. 2 Sensorimotor improvements after PBMT. **A, B** EAE clinical score (**A**) and latency to fall in rotarod test (**B**) for EAE and EAE treated with PBMT (EAE-PBMT) animals. Time windows that were considered for analysis: baseline (D0–D11), onset of symptoms (D12–D16), peak of symptoms (D17–D21), and recovery stage (D22–D28). **C** Linear regression of the normalized latency to fall as a function of EAE clinical score. **D** Mouse posture at onset (top) and peak (bottom) of the symptoms with anatomical labels. **E**, **F** Top. Anatomical parameters of interest: tail tip height (**E**); sacrum height between tail base and iliac crest (**F**); limb elongation during locomotion period (**G**). Bottom, average evolution of the parameters of interest across the main stages of disease progression for untreated (gray) and PBMT-treated (red) mice. **A**–**C** $n = 16$ EAE and $n = 12$ EAE-PBMT mice. (**E**–**G**) $n = 12$ EAE and $n = 8$ EAE-PBMT mice. All the data were analyzed using the nonparametric two-tailed Mann–Whitney U test and presented as mean ± SEM; *P < 0.05; **P < 0.01; ***P < 0.001

locomotion periods (Fig. 2G). The tail tip (Fig. 2E) and the back height (Fig. 2F) as well as the foot motion range (Fig. 2G) appeared as reliable markers of the EAE clinical score severity.

Moreover, postural deficits (Fig. 2D, F) and locomotor function (Fig. 2G), which exhibited no recovery in the absence of PBMT, significantly improved by the end of the second week of PBMT *(respectively: $p = 0.004$, $p = 0.047$, $p = 0.031$)*. Altogether, the data demonstrate that the EAE-induced functional deficits are significantly alleviated by PBMT.

PBMT decreases dorsal inflammation and axonal damages

To obtain insights into the cellular mechanisms by which PBMT decreases sensorimotor symptoms of EAE mice, we conducted longitudinal intravital spinal cord imaging of the axons and neuroinflammatory cells at microscopic resolution throughout the progression of the disease. For this purpose, we utilized triple fluorescent mice to visualize $Thy1^+$ neurons, $LysM^+$ peripheral innate leukocytes, and $CD11c^+$ resident activated microglia. We conducted longitudinal multicolor 3D microscopic imaging of the dorsal spinal cord (Fig. 3A, B), and cells were subsequently automatically segmented for quantitative analyses (Fig. S2). The green $LysM^+$ cells, collectively contributing to the peripheral component of inflammation, were categorized into circulating (Fig. 3C) and infiltrated (Fig. 3D) subtypes based on their vascular or parenchymal localization and shape. The yellow $CD11c^+$ cells were identified as an activated microglial cell subtype, part of the resident component of inflammation (Fig. 3E).

Three weeks after the surgery required to implant the glass window, all mice exhibited a low basal level of resident inflammation with virtually no signs of peripheral

inflammation (Fig. 3A–E). In healthy control mice receiving PBMT, these levels remained consistent over weeks showing that the inflammatory status of the dorsal spinal cord was unaffected by PBMT (Fig. S3). These levels were also stable during the initial 10 days (D0–D10) post-induction in EAE mice (Fig. 3A, B).

An acute peak of inflammation in EAE mice occurred at D14, characterized by high densities of circulating peripheral cells (Fig. 3C) and their extensive infiltration into the parenchyma (Fig. 3D). Subsequently, the peripheral inflammation diminished while a chronic inflammation appeared through the progressive activation of resident microglia from D21 to D28 (Fig. 3E). The sudden accumulation of inflammatory peripheral cells in the spinal cord at D14 coincided with a drastic loss of axons. This loss was quantified at different distances from the dorsal vein (Fig. 3F). Interestingly, axon losses were more pronounced in the vicinity of blood vessels (Fig. 3G–I), corresponding to locations of inflammatory plaques. Axonal numbers progressively recovered with the remission of peripheral inflammation (Fig. 3G).

PBMT exhibited very significant effects on (i) the initial recruitment of peripheral cells, (ii) subsequent axonal losses, and (iii) chronic microglial density. In the dorsal spinal cord, PBMT significatively resulted in a 70% reduction in the densities of circulating cells *($p < 0.015$)* (Fig. 3C) and a 50% decrease in infiltrated cells *($p < 0.003$)* (Fig. 3D) at D14. From D17 to D28, the residual densities of peripheral cells, both circulating and infiltrated, were unaltered with daily PBMT.

The acute reduction of peripheral inflammation by PBMT correlated with a significant 40% increase in axonal density at D14 compared with untreated EAE mice *($p < 0.003$)* (Fig. 3G). Notably, our longitudinal in vivo model outlined a correlation between peripheral inflammation and axonal degeneration (Fig. 4A), as well as chronic microglial reactivity (Fig. 4 B) and sensorimotor deficits (Fig. 4C). Additionally, the level of acute peripheral inflammation correlated with subsequent level of chronic microglial reactivity (Fig. 4B), which might have accounted for the delayed effect of PBMT on chronic microglial reactivity, as observed on D24 *($p < 0.027$)* and D28 *($p < 0.005$)* (Fig. 3E).

Collectively, the results highlight a link between peripheral inflammation and sensorimotor deficits through axonal degeneration and chronic microglial reactivity (Fig. 4D). They also demonstrate the potent anti-inflammatory and neuroprotective action of PBMT in the EAE MS model (Fig. 4A–C).

PBMT protects the whole spinal cord from acute inflammation and axonal damage

Since the intravital imaging was confined to the superficial dorsal spine, we sought to determine whether the effects of PBMT extended to the whole spinal cord. We elucidated the physiopathological impact of PBMT at the peak of EAE symptoms (D17) with a focus on its ventral region. To this end, we conducted histological analysis on coronal slices employing a five-color approach. Immunostaining against Iba1 (microglia) and GFAP (astrocytes) was utilized in addition to the three endogenous fluorophores to characterize the interplay between inflammatory foci and glial reactivity or axons (Fig. 5A, B).

At D17, EAE mice exhibited white matter (WM) axonal degeneration (Fig. 5C), which was associated with a substantial infiltration of peripheral cells, particularly in the ventral region of the spinal cord, where their density was twice that of the dorsal region (Fig. 5D). PBMT did not change the number of neuronal soma in the gray matter (GM) but resulted in diminished axonal loss *($p = 0.048$)* (Fig. 5C). This decreased axonal loss was concomitant with a significant attenuation (50%) of peripheral cells in the ventral region *($p = 0.009$)* (Fig. 5D) likely due to their reduced in-depth parenchymal infiltration *($p = 0.004$)* (Fig. 5E).

In terms of the glial contribution to inflammation, PBMT did not alter CD11c + densities (Fig. 5F). However, it globally reduced the density of Iba1$^+$ cells, particularly in the ventral region *($p = 0.006$)* (Fig. 5G), without modifying the proportion of CD11c$^+$ among the total Iba1$^+$ microglial population (Fig. 5H). Moreover, the microglial

(See figure on next page.)

Fig. 3 Anti-inflammatory and neuroprotective effect of PBMT evaluated via longitudinal and intravital microscopy. **A** Representative maximal intensity projection (MIP) of in vivo 2P z-stack of dorsal spinal cord images obtained from the same animals on days 0, 7, 10, 14, 17, 21, 24, and 28 for EAE (top) and EAE-PBMT (bottom) triple transgenic (Thy1-CFP//LysM-EGFP//CD11c-EYFP) mice**.** Scale bar, 200 µm. **B** Zoom of the gray and red boxes represented in **A**. Scale bar, 200 µm. **C**–**E** Evolution of the average cell densities for circulating peripheral LysM$^+$ cells (**C**), infiltrated peripheral LysM$^+$ cells (**D**), and resident CD11c$^+$cells (**E**) for EAE (gray) and EAE-PBMT (red) mice. Insets show examples of raw (left) or segmented (right) images for each cell subtype. **F** Neuronal component of a representative MIP image illustrating the protocol for multisite quantification of axon numbers at various distances from the dorsal vein: proximal (0–100 µm), medial (100–200 µm), distal (200–300 µm). **G**–**I** Evolution of the normalized axon numbers at different distances from the dorsal vein for EAE (gray) and EAE-PBMT (red) mice. **C**–**I** n = 8 mice for each group (EAE and EAE-PBMT). All data were analyzed using the nonparametric two-tailed Mann–Whitney U test and presented as mean ± SEM; *P < 0.05; **P < 0.01; ***P < 0.001; NS, not significant

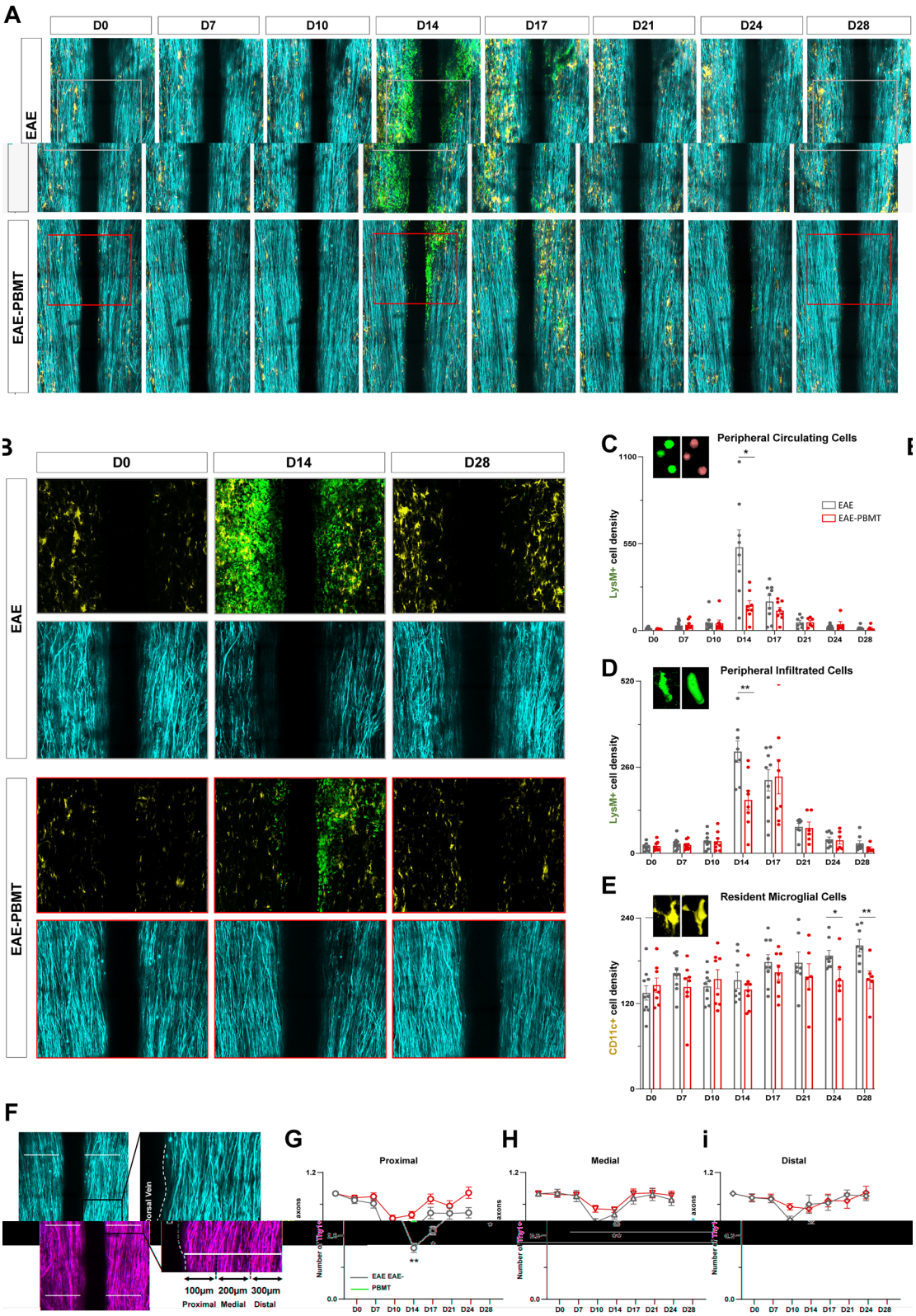

Fig. 3 (See legend on previous page.)

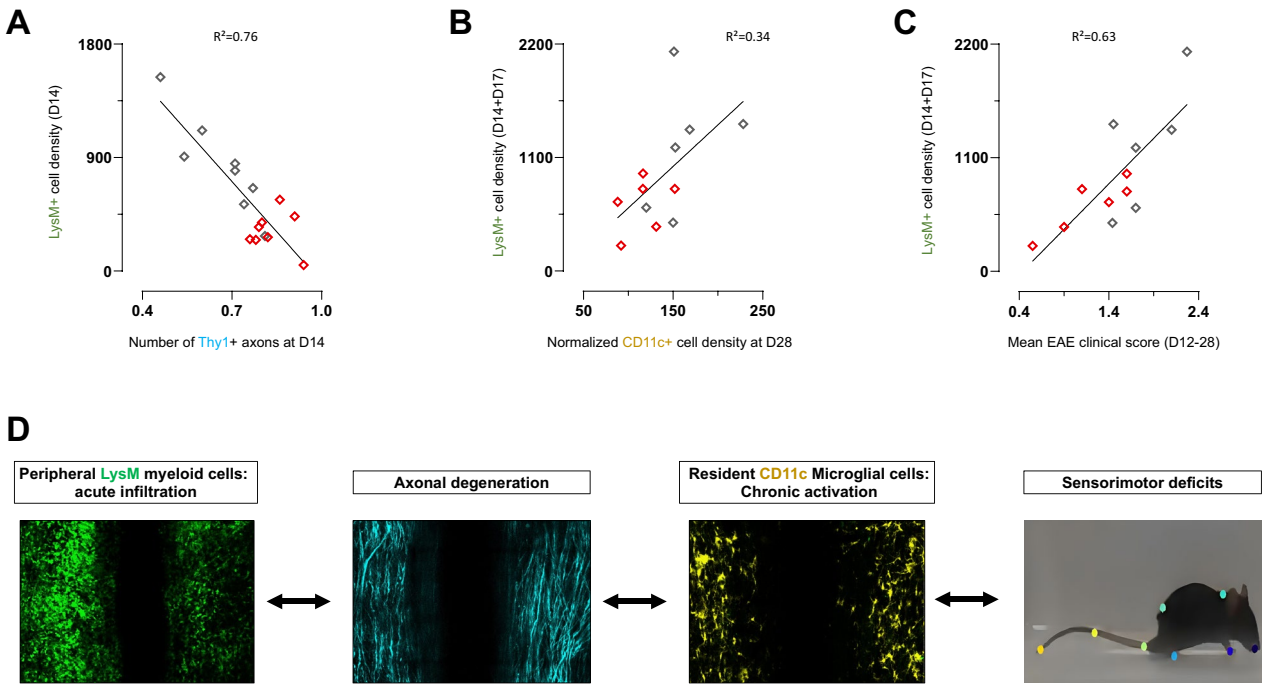

Fig. 4 Correlation between the dorsal intraspinal inflammatory status and axonal degeneration or sensorimotor deficits in EAE mice (**A**–**C**). Linear correlation between LysM$^+$ cell densities and axonal densities at D14 for all EAE and EAE-PBMT mice n = 16 (**A**). Linear correlation between the cell densities of LysM$^+$ cells at D14 and D17 and the densities of CD11c$^+$ cells actually observed at D28 for both EAE and EAE-PBMT mice (n = 12) (**B**). Linear correlation between the summed densities of LysM$^+$ cells at D14 and D17 and the average clinical score observed from D12 to D28 for both EAE and EAE-PBMT mice (n = 12) (**C**). Schematic representation using 2P images illustrating the correlations presented above (**D**)

phenotype switched from an activated amoeboid phenotype to a ramified resting state in response to PBMT (Fig. S4).

Using a GFAP level of expression as an index of astrocyte reactivity, we observed a 25% decrease in response to PBMT, mainly at the ventral level *($p < 0.001$)* (Fig. 5I) and in WM *($p < 0.001$)* (Fig. 5J). These changes in microglia morphologies and astrocyte reactivity resulting from PBMT did not significantly modify the number of contacts between astrocytes and microglia (Fig. 5K).

Altogether, these findings underscore a ventral effect of PBMT at the peak of the disease and support a dual effect on peripheral inflammation and glial reactivity.

PBMT protects the progressive spread of glial reactivity

To further elucidate the physiopathological impact of PBMT during the recovery phase of EAE, we conducted a comparable histological study at D28. We found a higher average axonal density in the WM in PBMT mice compared with untreated mice *($p = 0.046$)* (Fig. 6A–C). No alterations were observed in soma density within the GM (Fig. 6C). In agreement with the in vivo observations (Fig. 3A), inflammation at D28 was predominantly orchestrated by resident microglia rather than infiltrated peripheral cells (Fig. 6D–H). Although some foci of inflammatory peripheral cells

(See figure on next page.)

Fig. 5 Effects of PBMT in the ventral spinal regions on D17. **A** Representative confocal images of Thy1 (cyan), LysM (green), CD11c (yellow), Iba1 (red), and GFAP (blue) labeling in the spine of EAE (left) and EAE-PBMT (right) mice at D17. For each marker, whole slice expression (left column) is followed by two zoomed-in views focusing on the regions highlighted by white rectangles (middle and right columns). Scale bar, respectively, 300 µm, 100 µm, and 40 µm. **B** Raw and segmented views of cell subtypes. **C**–**K** Average densities in specific spinal regions for EAE (gray) and EAE-PBMT (red) mice. **C** Thy1$^+$ axons and soma in the white matter (WM) and gray matter (GM), respectively. **D** Dorsal and ventral densities of LysM$^+$ cells. **E** Average LysM$^+$ cell distance to the surface. **F**, **G** Dorsal and ventral densities of CD11c$^+$ (**F**) or Iba1$^+$ (**G**) cells. **H** Percentage of CD11c$^+$ among the total Iba1$^+$ cells. **I**, **J** Percentage of the GFAP$^+$ surface in the dorsal and ventral regions (**I**), in the WM or GM (**J**). **K** Proportion of Iba1$^+$ cells contacting GFAP$^+$ processes (**C**–**K**) $n = 13$ slices for three EAE and for three EAE-PBMT mice. Data presented as mean ± SEM and analyzed by nonparametric two-tailed Mann–Whitney U test; *P < 0.05; **P < 0.01; ***P < 0.001; NS, not significant

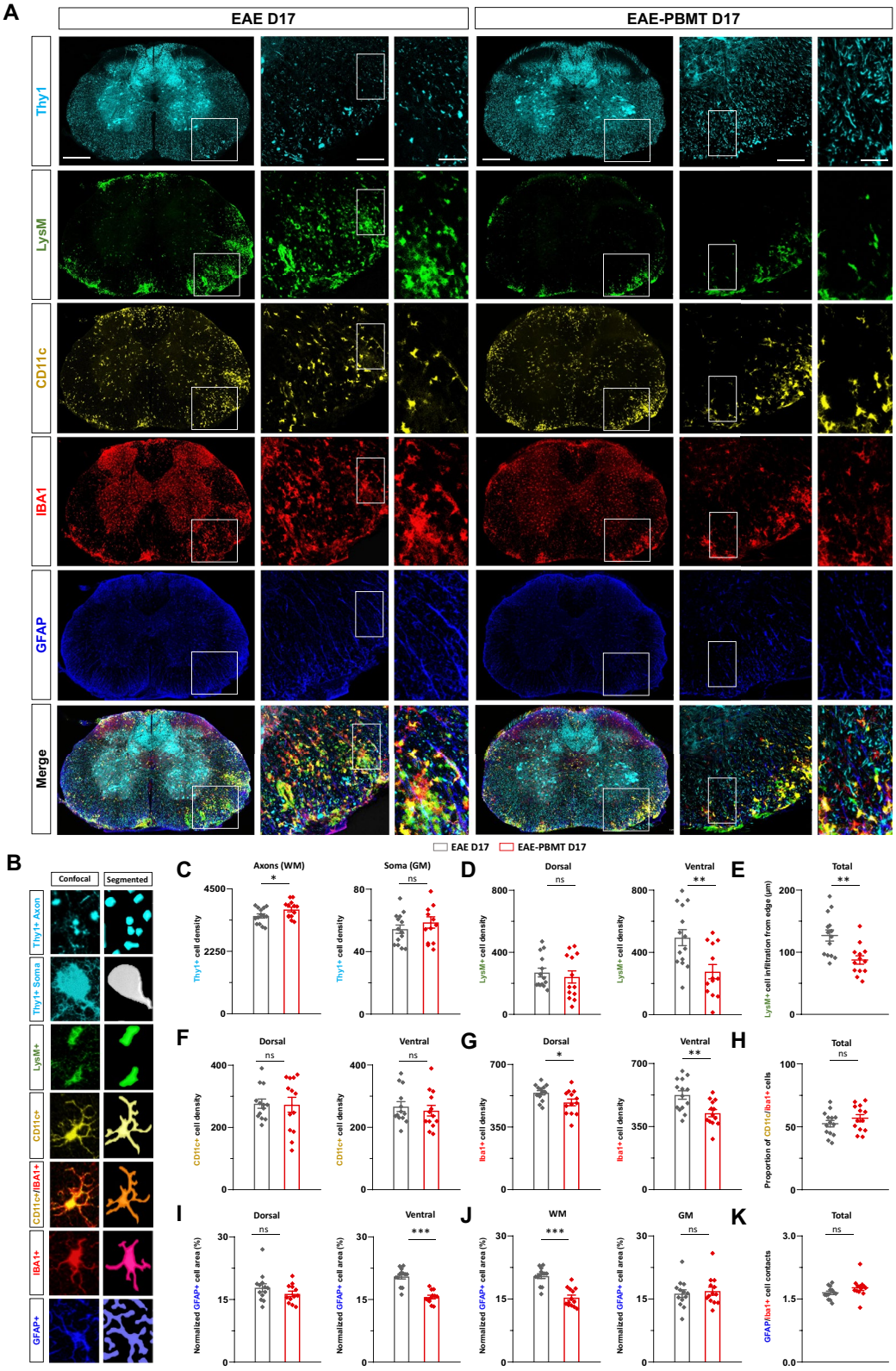

Fig. 5 (See legend on previous page.)

persisted, mostly in the ventral part, their presence was significantly decreased by PBMT *($p = 0.015$)* (Fig. 6D).

At this later stage, both CD11c$^+$ (Fig. 6F) and Iba1$^+$ (Fig. 6G) microglia were significantly diminished by PBMT across the entire spinal cord compared with D17, with a more pronounced impact in the ventral region *(CD11c$^+$: $p < 0.001$, Iba1$^+$: $p = 0.040$)*. Iba1$^+$ cells were predominantly concentrated in the GM, while CD11c + cells tended to accumulate in the WM; PBMT demonstrated effectiveness in both regions (Fig. S5). The proportion of reactive CD11c$^+$ microglia among Iba1$^+$ cells was, moreover, globally lowered by PBMT *($p < 0.001$)* (Fig. 6H). GFAP was extensively expressed in all spinal regions of EAE mice and PBMT globally reduced this reactivity, especially within the GM (Fig. 6I, J) *(respectively, $p = 0.046$; $p = 0.050$, $p = 0.041$; $p = 0.005$)*. The number of contacts between astrocytes and microglia, still remained unaffected by PBMT (Fig. 6K). Importantly, such prolonged PBMT did not alter the inflammatory status of the spinal cord in healthy control mice (Fig. S6).

In summary, the findings demonstrate that prolonged PBMT exerts beneficial effects on EAE-induced chronic inflammation and glial reactivity. It prevents the spread of glial activation from WM to GM and does not affect healthy spinal tissue.

PBMT decreases EAE-induced neuronal hyperexcitability

To bridge the gap between the anti-inflammatory effects of PBMT and its functional consequences on sensorimotor deficits, we investigated the electrophysiological properties of the dorsal horn sensory neurons (lamina I–II) and of the ventromedial premotor neurons (lamina X) from lumbar slices on D28 (Fig. 7A, B). We observed hyperexcitability of these neurons in EAE mice, characterized by an increased firing frequency in response to a depolarizing current (F-I gain) ($p = 0.011$) (Fig. S7A); ($p = 0.031$) (Fig. S7B). These electrophysiological properties were consistent with the high degree of inflammation observed in the regions of recordings (Figs. 6A, S5A).

Interestingly, the PBMT was sufficient to decrease the EAE-induced hyperexcitability for both neuronal subtypes (Fig. 7C–H), while PBMT was completely ineffective in control mice (Fig. S8). Therefore, PBMT on EAE mice resulted in (i) a more hyperpolarized resting membrane potential ($p = 0.001$, $p = 0.002$ for dorsal and ventral neurons, respectively), (ii) a recruitment at higher currents related to an increased rheobase ($p < 0.001$ for ventral neurons), and (iii) a lower maximum spiking frequency for both neuronal populations ($p = 0.046$, $p = 0.014$ for dorsal and ventral neurons, respectively) (Fig. 7E, F). Importantly, PBMT reduced neuronal excitability mainly through the F-I gain for both neuronal types from EAE mice. This effect was more pronounced for premotor neurons ($p = 0.008$, $p < 0.001$ for dorsal and ventral neurons, respectively)(Fig. 7G, H).

Altogether, these results highlight the role of PBMT in preventing EAE neuronal hyperexcitability.

Discussion

We performed a longitudinal and multimodal study of the effects of PBMT on a rodent EAE MS model using complementary tools such as intravital imaging on a unique multifluorescent transgenic mouse line, behavioral analyses to assess in vivo functional deficits, five-color histological imaging, and ex vivo electrophysiological patch-clamp recordings in adult spinal slices. We highlighted a robust PBMT beneficial effect on sensorimotor deficits from EAE mice highly correlated to the dynamics of inflammation as evaluated in the dorsal spinal cord. More precisely, we further demonstrated that PBMT (i) displayed a dual anti-inflammatory effect, both on the infiltration of myeloid cells during the onset phase and on glial reactivity during the recovery phase; (ii) protected from axonal loss; and (iii) counterbalanced the EAE-induced neuronal hyperexcitability.

To evaluate whether the PBMT might be envisaged for patients with relapsing–remitting MS, we started the PBM irradiation on our EAE-induced mice at the occurrence of the first clinical symptoms. PBMT stimulation parameters were defined from successful preclinical studies [11]. Notably, we verified on control mice (not EAE-induced) that such PBMT conditions and repeated

(See figure on next page.)

Fig. 6 PBMT decreases chronic inflammation and promotes axonal regeneration on D28. **A** Representative confocal images of Thy1 (cyan), LysM (green), CD11c (yellow), Iba1 (red), and GFAP (blue) labeling in the spine of EAE (left) and EAE-PBMT (right) mice at D28. For each marker, whole slice expression (left column) is followed by two zoomed-in-views focusing on the regions highlighted by white rectangles (middle and right columns). Scale bar, respectively, 300 µm, 100 µm, and 40 µm. **B** Regionalization views of the segmented cell subtypes. **C**–**K** Average densities in specific spinal regions for EAE (gray) and EAE-PBMT (red) mice. **C** Thy1$^+$ axons and soma in the white matter (WM) and gray matter (GM), respectively. **D** Dorsal and ventral densities of LysM$^+$ cells. **E** Peripheral inflammation at D17 gave way to microglia inflammation at D28. **F**, **G** Dorsal and ventral densities of CD11c$^+$ (**F**) or Iba1$^+$ (**G**) cells. **H** Percentage of CD11c$^+$ among the total Iba1$^+$ cells. **I**, **J** Percentage of the GFAP$^+$ surface in the dorsal and ventral regions (**I**), in the WM or GM (**J**). **K** Proportion of Iba1$^+$ cells contacting GFAP$^+$ processes **(C–K)** $n = 12$ slices for three EAE and for three EAE-PBMT mice. Data presented as mean ± SEM and analyzed by nonparametric two-tailed Mann–Whitney U test; *P < 0.05; **P < 0.01; ***P < 0.001; NS, not significant

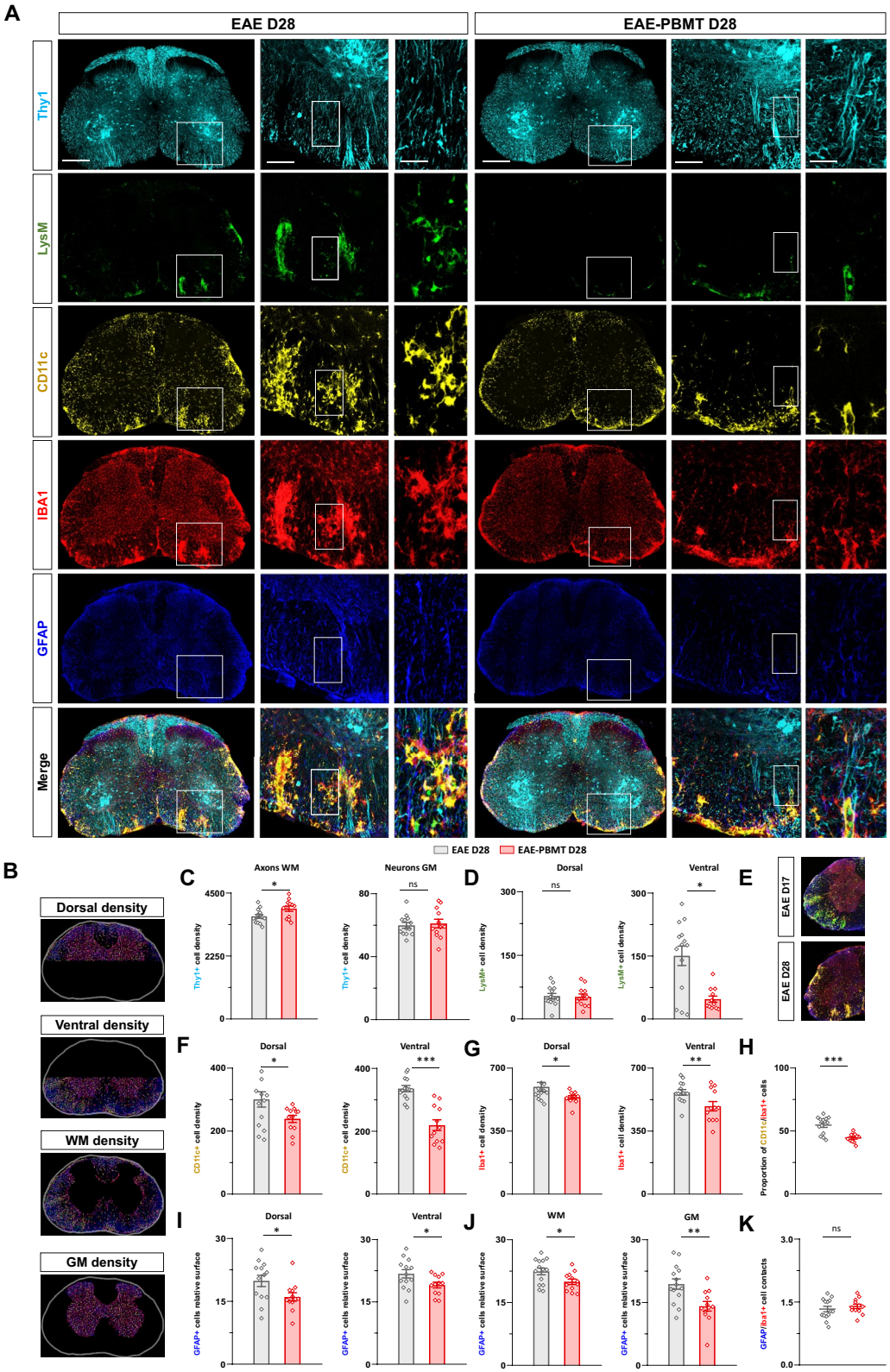

Fig. 6 (See legend on previous page.)

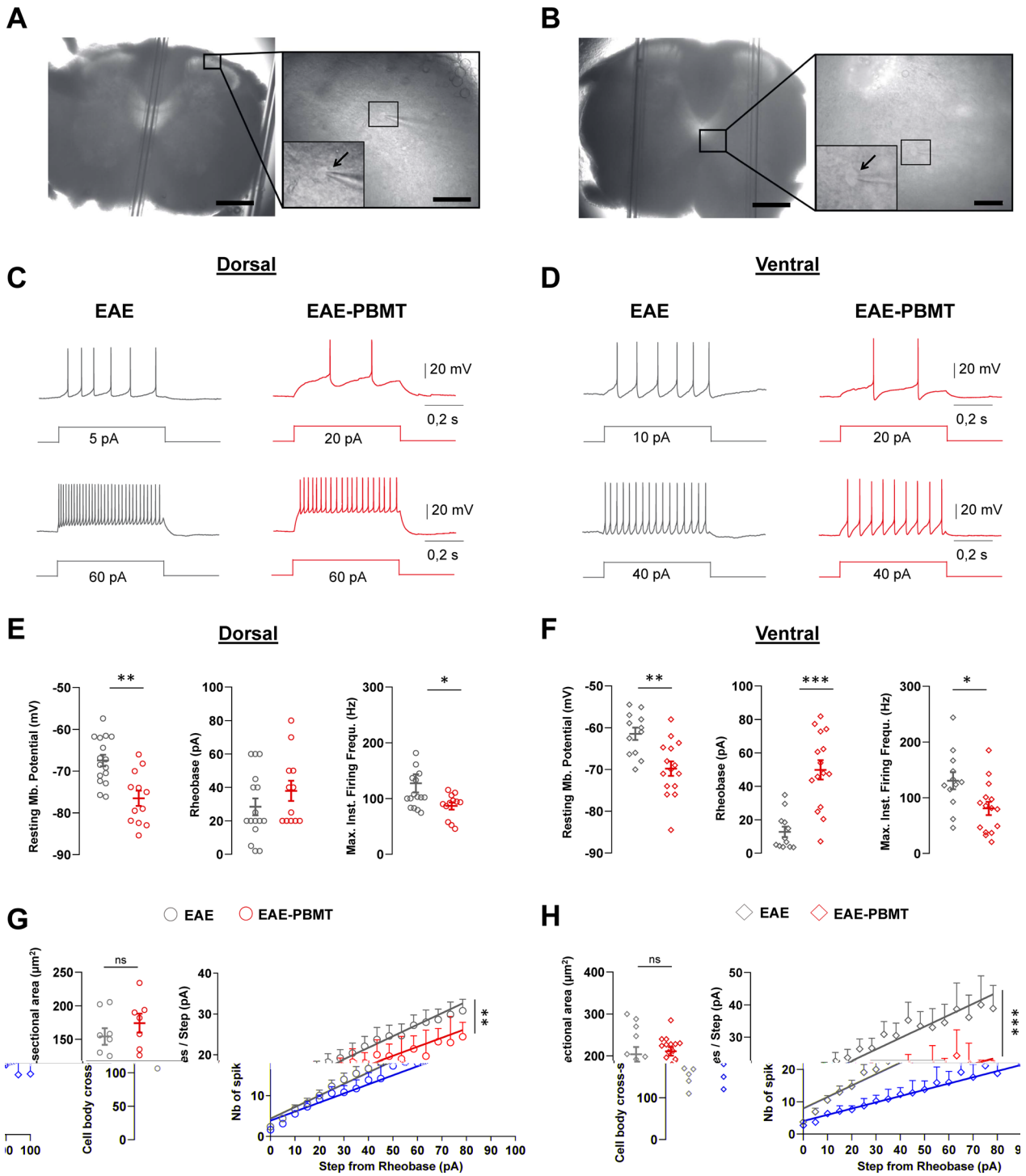

Fig. 7 PBMT decreases the EAE-induced hyperexcitability of lumbar interneurons. **A**, **B** Bright field images of acute lumbar slices with patch-clamp recording pipette. Scale bar, 400 µm. Inset: High magnification images of interneurons in the dorsal horn (DH), scale bar, 50 µm, (**A**) or ventro-medial (VM) premotor region (**B**). **C**, **D** Representative membrane potential responses to depolarizing pulses at rheobase (top) or twice the rheobasic strength (bottom) for DH (**C**) or VM (**D**) neurons from EAE (gray) or EAE-PBMT (red) mice. **E**, **F** Quantification of the resting membrane potentials (left), rheobase (middle), and maximum firing frequency (right) of DH (**E**) or VM (**F**) neurons from EAE (gray) or EAE-PBMT (red) mice. **G**, **H** Cell body cross-sectional area (left) and number of action potentials induced by depolarizing current steps (right) for the same DH (**G**) or VM (**H**) neurons as in **E**, **F**. **E**–**H**: n = 16 DH and n = 12 VM neurons from six EAE mice and n = 12 DH and n = 15 VM from seven EAE-PBMT mice. Data presented as mean ± SEM and analyzed by nonparametric two-tailed Mann–Whitney U test (**E, F, G** left, **H** left) or slope comparisons test of simple linear regressions (**G** right**, H** right); *P < 0.05; **P < 0.01; ***P < 0.001; NS, not significant. See also Figs. S7, S8

irradiations were not inducing identifiable cellular modifications in the spinal cord tissue. We assessed the sensorimotor deficits of the EAE-control and PBMT-treated mice by independently measuring postural and locomotor deficits throughout the 28 days post-induction. PBMT delivered at the disease onset demonstrated efficacy in significantly attenuating the peak of deficits while improving locomotor function by the end of the first week of PBMT.

Since sensorimotor functions are controlled by neuronal activity, we investigated the effects of PBMT on the evolution of axonal densities in the dorsal spinal cord from disease onset to D28 as well as its effect on the electrophysiological properties of neurons on D28, namely the sensory neurons in the dorsal horn and the premotor neurons in the ventromedial area. On D14, we observed by intravital imaging that the loss of axons was reduced by nearly 50% in the PBMT-treated mice**.** Axonal densities were also consistently enhanced throughout the spinal cord during the recovery phase as evidenced by postmortem histology on D17 and D28. Whereas EAE has been associated with increased dorsal root ganglion excitability [41], we describe here, for the first time, the presence of EAE-induced hyperexcitability of at least two central nervous system (CNS) spinal neuronal subtypes associated with sensorimotor functions [42]. Spinal neuron hyperexcitability has been associated with sensory [43, 44] and motor deficits [45, 46] in response to spinal cord injury; it is thus likely responsible for the functional deficits observed in our EAE model of MS. Importantly, PBMT countered this hyperexcitability and stabilized the neuronal electrophysiological properties. These observations thus infer that PBMT protects from axonal degeneration and neuronal dysfunctions. It remains to be seen whether PBMT also has an effect on myelinization of axons.

Although we cannot exclude that such beneficial outcome is due to a local and direct effect of the irradiation on neurons, several of our observations, as well as previous work, support the view that most of the effect is indirect and attributable to the systemic modulation of cellular interactions.

First, a strong effect of PBMT was observed in the ventral motor networks, where photons struggled to penetrate, compared with the dorsal regions that are more directly exposed to light after spinal glass window implantation. Second, since astrocytes are interconnected by gap junctions into widespread glial networks [47] and modulate neuronal excitability in both the dorsal [44] and ventral [48] spinal cord, dorsal illumination could thus indirectly impact ventral neuronal excitability. However, the effect of PBMT on glial reactivity, both astrocytic and microglial, was also larger in the ventral region than in the dorsal one. Third, glial reactivity can disturb the electrophysiological properties of neurons [49, 50] due to (i) increased secretion of cytokines or excitatory metabolites [51, 52] or (ii) K^+ and glutamate dyshomeostasis [53]. Thus, the glial reactivity that we highlighted in this study through astrocytic GFAP and microglial CD11c labeling could explain the observed EAE-induced neuronal hyperexcitability. The fact that PBMT limited the glial reactivity in the recovery phase of EAE mice likely explains the decrease of neuronal hyperexcitability and the subsequent improvement at the behavioral level in EAE-PBMT-treated mice. Finally, we observed a significant and early inhibitory effect of PBMT on the infiltrating peripheral inflammatory cells. Under physiological conditions, the blood–brain barrier (BBB) efficiently controls their entrance into the CNS [54, 55]**,** while under pathological conditions such as in EAE and MS, neutrophiles and monocytes infiltrate the CNS and collaborate with reactive microglia to promote inflammatory axonal damage that leads to paralysis [56, 57]. This recruitment from the systemic circulation into the CNS involves chemokines secreted by spinal astrocytes or microglia in pathological conditions, which facilitate the disruption of tight junctions, permeabilization of the BBB, and transmigration of inflammatory cells into the parenchyma [58–61]**.** In our study, PBMT decreased both the reactivity of microglia and astrocytes and the infiltration of peripheral inflammatory cells during the onset phase of EAE. A possible explanation of the effect of PBMT could therefore be that the light-induced dampening of chemokine release resulted in the maintenance of BBB integrity.

The mechanism by which PBMT may modulate inflammation through glial reactivity, however, remains unclear. Some data support a direct action of light on glia [62, 63] and peripheral inflammatory cells [64] in an intensity-dependent manner [65]. Our data might instead support a predominant systemic action of superficial PBMT on skin [66] and blood vessels [67] whose immunoregulatory role and endocrine release might impact the deepest CNS compartments using the dense networks of blood [68] and glymphatic [69] vessels. It was, for example, shown that exosomes emanating from every cell type of the body circulate in the blood of MS subjects and regulate inflammatory processes [70, 71]. Such a hypothesis was raised as a possible explanation of the neuroprotective effect of PBMT when applied on the leg or abdomen in a nonhuman primate model of Parkinson's disease [7].

In this view, exosomes released from the enteric system itself might similarly regulate the inflammatory status of the spinal cord. The device used in this study indeed relies on a dorsoventral PBMT that may trigger the gut-brain axis [72]**.** Over the past decade, numerous

studies have suggested the role of this complex network as a key player in immunity [73, 74] and showed that the gut microbiota can modulate immune responses relevant to MS pathogenesis [75, 76]. In further support of this hypothesis, PBMT simultaneously targeted to the brain and to the enteric system efficiently dampened brain inflammation and improved cognitive functions in a rodent model of Alzheimer's disease, while brain stimulation alone was ineffective [11].

Although preclinical animal models represent a required step to justify and support clinical trials, subtle differences in the immune systems of mice and humans might have to be taken into account [77]. Importantly, the treatment protocol used here has not identified a specific therapeutic window that maximizes the PBMT effects. To optimize therapeutic protocols, additional experiments are necessary to decide whether the duration of treatment could be stopped after the peak of inflammation while allowing for a long-lasting protection of neuronal attacks or whether both dorsal and ventral illuminations are necessary until complete remission. Finally given its efficacy in dorsoventral application for treating MS, it would be valuable to explore the effects of PBMT on brain regions where inflammation is elevated in MS.

Conclusion

Our preclinical study provides a robust demonstration of PBMT efficacy as a new, efficient, and complementary therapeutic strategy to treat EAE. PBMT can be applied in a non-invasive and safe way while showing important benefits on sensorimotor functions in pathological conditions without side effects. It can be easily applied in humans since PBMT offers the major advantage of modulating inflammation without complete and detrimental immunosuppression. Chronic treatment with PBMT would thus allow patients to maintain their immune defenses while dampening pathological inflammation, not only observed in MS but also in many other chronic inflammatory diseases.

Supplementary Information

The online version contains supplementary material available at https://doi.org/10.1186/s12974-024-03294-2.

Additional file 1: Figure S1. PBMT does not alter functional outcomes and locomotor performances in healthy control mice. (A–B) EAE clinical score (A) and rotarod latency to fall (B) for control (CTRL, n = 8) and CTRL treated by PBMT (CTRL-PBMT n = 8). Data presented as mean ± SEM and analyzed by nonparametric two-tailed Mann–Whitney U test; *P < 0.05; **P < 0.01; ***P < 0.001; NS, not significant.

Additional file 2: Figure S2. Automated cell segmentation of intravital images of the inflammatory dorsal spinal cord. (A) Representative maximal intensity projection (MIP) of a z-stack of images acquired by in vivo 2P on a triple transgenic Thy1-CFP//LysM-EGFP//CD11c-EYFP) EAE mouse at D14. Scale bar, 400 µm. (B) Set of segmented images corresponding to the data presented in (A). High magnification image sets of the three inflammatory cell subtypes: the circulating LysM$^+$ cells (red, left), the infiltrated LysM$^+$ cells (green, middle), and the CD11c$^+$ resident cells (yellow, right). Scale bar, 20 µm.

Additional file 3: Figure S3. PBMT does not affect basal inflammatory state in healthy control mice. (A) Representative maximal intensity projection (MIP) of in vivo 2P z-stack of dorsal spinal cord images obtained from two animals on days 0, 7, 10, 14, 17, 21, 24, and 28 for one CTR (top) and one CTR-PBMT (bottom) triple transgenic (Thy1-CFP//LysM-EGFP//CD11c-EYFP) mice. Scale bar, 200 µm. (B, C) Evolution of the average cell densities for all peripheral LysM$^+$ cells (circulating and infiltrated) (B) and resident CD11c$^+$ cells (C) for CTR (gray, n = 4) and CTR-PBMT (red, n = 4) mice. Data presented as mean ± SEM and analyzed by nonparametric two-tailed Mann–Whitney U test; *P < 0.05; **P < 0.01; ***P < 0.001; NS, not significant.

Additional file 4: Figure S4. Microglial change of morphological phenotype induced by PBMT in EAE mice. (A) Representative maximal intensity projection (MIP) of z-stacks of confocal images showing intraspinal CD11c$^+$ cells on coronal slices of EAE (top) and EAE-PBMT (bottom) mice at D17. Scale bar, 50 µm. (B, C) Cell circumference (left), cell surface (middle), and cell sphericity (right) of the CD11c$^+$ (B) and Iba1$^+$ (C) cells from EAE (gray, n = 3) and EAE-PBMT (red, n = 3) mice. Data presented as mean ± SEM and analyzed by nonparametric two-tailed Mann–Whitney U test; *P < 0.05; **P < 0.01; ***P < 0.001; NS, not significant.

Additional file 5: Figure S5. PBMT reduces the glial reactivity also in the gray matter (GM) on D28 in EAE mice. (A) Representative maximal intensity projection (MIP) of z-stacks of confocal images showing coronal slices of spinal cord stained for Iba1 (red) and GFAP (blue) in addition to the triple endogenous staining for Thy1 (cyan), LysM (green), and CD11c (yellow) for EAE (left) and EAE-PBMT (right) mice on D28. Scale bar, 300 µm. White boxes highlight the ventro-medial region and the dorsal horn, where neurons were recorded with patch-clamp. High magnifications of the distribution of each marker in these boxes (below) Scale bar, 100 µm. (B, C) Densities of cells in the WM (left) and in the GM (right) for CD11c$^+$ cells (B) and Iba1$^+$ cells (C). (D) Percentage of the GFAP$^+$ spinal surface in regions where neurons were recorded with patch-clamp. *N* = 12 slices from three EAE and three EAE-PBMT mice. Data presented as mean ± SEM and analyzed by nonparametric two-tailed Mann–Whitney U test; *P < 0.05; **P < 0.01; ***P < 0.001; NS, not significant.

Additional file 6: Figure S6. PBMT does not affect glial reactivity or neuronal density in healthy control mice. (A) Representative maximal intensity projection (MIP) of z-stacks of confocal images showing coronal slices of spinal cord stained for Iba1 (red) and GFAP (blue) in addition to the triple endogenous staining for Thy1 (cyan), LysM (green), and CD11c (yellow) for control (CTRL, left) and control treated by PBMT (CTRL-PBMT, right) mice 28 days after the initial 3 weeks postsurgical recovery. Scale bar, 300 µm. (B) Average densities of Thy1$^+$ axons in the WM (left) and of Thy1$^+$ somas in the GM (right) for CTRL and CTRL-PBMT mice. (C) Average density of LysM + cells. (D–F) Average densities of CD11c$^+$ cells (D), Iba1$^+$ cells (E), and relative GFAP$^+$ surface (F). *n* = 8–9 slices from three CTRL and three CTRL-PBMT mice. Data presented as mean ± SEM and analyzed by nonparametric two-tailed Mann–Whitney U test; *P < 0.05; **P < 0.01; ***P < 0.001; NS, not significant.

Additional file 7: Figure S7. Neuronal hyperexcitability in EAE mice compared with controls (A–D). (A, B) Number of action potentials induced by depolarizing current steps (right) for the dorsal horn (A) or ventral premotor (B) neurons. For this electrophysiological analysis, *n* = 9 dorsal and *n* = 6 ventral neurons from five CTRL untreated mice and *n* = 12 dorsal and *n* = 15 ventral neurons from six EAE mice. Data presented as mean ± SEM and analyzed by slope comparisons test of simple linear regressions (A, B); *P < 0.05; **P < 0.01; ***P < 0.001; NS, not significant.

Additional file 8: Figure S8. PBMT does not affect neuronal excitability in healthy control mice. (A, B) Representative membrane potential

responses to depolarizing pulses at rheobase (top) or twice the rheobasic strength (bottom) for dorsal horn (a) or ventral premotor (B) neurons from CTRL (gray) or CTRL-PBMT (red) mice. (C, D) Quantification of the resting membrane potentials (left), rheobase (middle), and maximum firing frequency (right) of dorsal horn (C) or ventral premotor (D) neurons from EAE (black) CTRL (gray) or CTRL-PBMT (red) mice. (E, F) Cell body cross-sectional area (left) and number of action potentials induced by depolarizing current steps (right) for the same dorsal horn (E) or ventral premotor (F) neurons as in (C–D). For this electrophysiological analysis, $n=9$ dorsal and $n=6$ ventral neurons from five CTRL untreated mice and $n=5$ dorsal and $n=8$ ventral neurons from four CTRL-PBMT treated mice. Data presented as mean ± SEM and analyzed by nonparametric two-tailed Mann–Whitney U test (C–D, E left, F left) or slope comparisons test of simple linear regressions (E right, F right); *P < 0.05; **P < 0.01; ***P < 0.001; NS, not significant.

Acknowledgements
The authors thank Dr. Guillaume Champleboux from REGEnLIFE for his engineering and logistic support with the RGn535 preclinical device; Dr. Alberto Lombardini from INT imaging facility for the tuning and maintenance of optical microscopes; Dr. Erica Lopez and Dr. Mourad Mekaouche from CEFOS animal facility at AMU for their assistance with and advice on animal experimentation and surgical optimization; Dr. Emilie Pecchi and Elsa Lévy for technical assistance on histology and immunostaining.

Author contributions
Conceptualization: G.B., J.T., G.R., R.B., F.D. Methodology: V.E., D.R., G.B., R.B., F.D. Investigation: V.E., R.B. Visualization: V.E., D.R., R.B., F.D. Funding acquisition: G.B., R.B., F.D. Project administration: R.B., F.D. Supervision: G.B., R.B., F.D. Writing—original draft: V.E., G.R., R.B., F.D. Writing—review and editing: V.E., D.R., G.B., J.T., G.R., R.B., F.D.

Funding
This work was supported by REGEnLIFE and the French Agence Nationale pour la Recherche Technologique (ANRT) through a CIFRE PhD fellowship to V. E. (G. B., R. B., F. D.), Agence Nationale pour la Recherche (ANR) grant 18-CE19-0029-02 (F. D.), ARSEP 1248 (F. D.), and core support from IUF, AMU, and CNRS, grant "Fonds d'investissement, INT-2023" (F.D. and R.B.).

Data availability
Data, codes, and materials used in the analysis and presented in the figures are available upon request made to the corresponding authors.

Declarations

Ethics approval and consent to participate
All experimental procedures were performed in accordance with the French legislation and in compliance with the European Community Council Directive of November 24, 1986 (86/609/EEC), for the care and use of laboratory animals. The research was authorized by the Direction Départementale des Services Vétérinaires des Bouches-du-Rhône (license D-13-055-21) and approved by the National Committee for Ethics in Animal Experimentation and the local ethics committee (Comité d'Ethique en Neurosciences INT-Marseille, CE71 Nb A1301404 [project authorization APAFIS#31909 and CE14 project authorization APAFIS#30760]).

Competing interests
G. B. is a member of the company REGEnLIFE and owns equity. J. T. is a consultant for REGEnLIFE. V.E., D. R., G. R., R. B., and F.D. are members of AMU and declare that they have no financial interests that could be perceived as being a conflict of interest or to influence the work reported in this paper.

Received: 2 September 2024 Accepted: 11 November 2024
Published online: 18 December 2024

References

1. Soheilifar S, Fathi H, Naghdi N. Photobiomodulation therapy as a high potential treatment modality for COVID-19. Lasers Med Sci. 2021;36:935–8.
2. Bian J, Liebert A, Bicknell B, Chen X-M, Huang C, Pollock CA. Therapeutic potential of photobiomodulation for chronic kidney disease. IJMS. 2022;23:8043.
3. Cardoso FDS, Salehpour F, Coimbra NC, Gonzalez-Lima F, Gomes Da Silva S. Photobiomodulation for the treatment of neuroinflammation: a systematic review of controlled laboratory animal studies. Front Neurosci. 2022;16:1006031.
4. Lin H, Li D, Zhu J, Liu S, Li J, Yu T, et al. Transcranial photobiomodulation for brain diseases: review of animal and human studies including mechanisms and emerging trends. Neurophoton. 2024. https://doi.org/10.1117/1.NPh.11.1.010601.full.
5. Ma H, Du Y, Xie D, Wei ZZ, Pan Y, Zhang Y. Recent advances in light energy biotherapeutic strategies with photobiomodulation on central nervous system disorders. Brain Res. 2024;1822: 148615.
6. Reinhart F, Massri NE, Darlot F, Torres N, Johnstone DM, Chabrol C, et al. 810nm near-infrared light offers neuroprotection and improves locomotor activity in MPTP-treated mice. Neurosci Res. 2015;92:86–90.
7. Gordon LC, Martin KL, Torres N, Benabid A, Mitrofanis J, Stone J, et al. Remote photobiomodulation targeted at the abdomen or legs provides effective neuroprotection against parkinsonian MPTP insult. Eur J Neurosci. 2023;57:1611–24.
8. Muili KA, Gopalakrishnan S, Meyer SL, Eells JT, Lyons J-A. Amelioration of experimental autoimmune encephalomyelitis in C57BL/6 mice by photobiomodulation induced by 670 nm light. PLoS ONE. 2012;7:e30655.
9. Muili KA, Gopalakrishnan S, Eells JT, Lyons J-A. Photobiomodulation induced by 670 nm light ameliorates MOG35-55 induced EAE in female C57BL/6 mice: a role for remediation of nitrosative stress. PLoS ONE. 2013;8:e67358.
10. Gonçalves ED, Souza PS, Lieberknecht V, Fidelis GSP, Barbosa RI, Silveira PCL, et al. Low-level laser therapy ameliorates disease progression in a mouse model of multiple sclerosis. Autoimmunity. 2016;49:132–42.
11. Blivet G, Meunier J, Roman FJ, Touchon J. Neuroprotective effect of a new photobiomodulation technique against $A\beta_{25-35}$ peptide-induced toxicity in mice: novel hypothesis for therapeutic approach of Alzheimer's disease suggested. Alzheimer's Dementia Transl Res Clin Intervent. 2018;4:54–63.
12. Monteiro F, Carvalho Ó, Sousa N, Silva FS, Sotiropoulos I. Photobiomodulation and visual stimulation against cognitive decline and Alzheimer's disease pathology: a systematic review. A&D Transl Res & Clin Interv. 2022;8: e12249.
13. Blivet G, Relano-Gines A, Wachtel M, Touchon J. A randomized, double-blind, and sham-controlled trial of an innovative brain-gut photobiomodulation therapy: safety and patient compliance. JAD. 2022;90:811–22.
14. Silva T, Fragoso YD, Destro Rodrigues MFS, Gomes AO, Da Silva FC, Andreo L, et al. Effects of photobiomodulation on interleukin-10 and nitrites in individuals with relapsing-remitting multiple sclerosis—randomized clinical trial. PLoS ONE. 2020;15:e0230551.
15. Hamblin MR. Mechanisms and mitochondrial redox signaling in photobiomodulation. Photochem Photobiol. 2018;94:199–212.
16. Joniová J, Gerelli E, Wagnières G. Study and optimization of the photobiomodulation effects induced on mitochondrial metabolic activity of human cardiomyocytes for different radiometric and spectral conditions. Life Sci. 2024;351: 122760.
17. Amaroli A, Clemente Vargas MR, Pasquale C, Raffetto M, Ravera S. Photobiomodulation on isolated mitochondria at 810 nm: first results on the efficiency of the energy conversion process. Sci Rep. 2024;14:11060.
18. Pope NJ, Denton ML. Differential effects of 808-nm light on electron transport chain enzymes in isolated mitochondria: implications for photobiomodulation initiation. Mitochondrion. 2023;68:15–24.
19. Foo ASC, Soong TW, Yeo TT, Lim K-L. Mitochondrial dysfunction and Parkinson's disease—near-infrared photobiomodulation as a potential therapeutic strategy. Front Aging Neurosci. 2020;12:89.
20. Charabati M, Wheeler MA, Weiner HL, Quintana FJ. Multiple sclerosis: neuroimmune crosstalk and therapeutic targeting. Cell. 2023;186:1309–27.
21. Pozzilli C, Pugliatti M, Vermersch P, Grigoriadis N, Alkhawajah M, Airas L, et al. Diagnosis and treatment of progressive multiple sclerosis: a position paper. Euro J Neurol. 2023;30:9–21.

22. Harirchian MH, Fatehi F, Sarraf P, Honarvar NM, Bitarafan S. Worldwide prevalence of familial multiple sclerosis: a systematic review and meta-analysis. Mult Scler Relat Disord. 2018;20:43–7.
23. Patsopoulos NA. Genetics of multiple sclerosis: an overview and new directions. Cold Spring Harb Perspect Med. 2018;8: a028951.
24. Barrie W, Yang Y, Irving-Pease EK, Attfield KE, Scorrano G, Jensen LT, et al. Elevated genetic risk for multiple sclerosis emerged in steppe pastoralist populations. Nature. 2024;625:321–8.
25. Schroeter CB, Huntemann N, Bock S, Nelke C, Kremer D, Pfeffer K, et al. Crosstalk of microorganisms and immune responses in autoimmune neuroinflammation: a focus on regulatory T cells. Front Immunol. 2021;12: 747143.
26. Thomas OG, Olsson T. Mimicking the brain: Epstein-Barr virus and foreign agents as drivers of neuroimmune attack in multiple sclerosis. Front Immunol. 2023;14:1304281.
27. Lanz TV, Brewer RC, Ho PP, Moon J-S, Jude KM, Fernandez D, et al. Clonally expanded B cells in multiple sclerosis bind EBV EBNA1 and GlialCAM. Nature. 2022;603:321–7.
28. Bjornevik K, Cortese M, Healy BC, Kuhle J, Mina MJ, Leng Y, et al. Longitudinal analysis reveals high prevalence of Epstein-Barr virus associated with multiple sclerosis. Science. 2022;375:296–301.
29. Bakhshi A, Eslami N, Norouzi N, Letafatkar N, Amini-Salehi E, Hassanipour S. The association between various viral infections and multiple sclerosis: an umbrella review on systematic review and meta-analysis. Rev Med Virol. 2024;34: e2494.
30. Wiendl H, Gold R, Berger T, Derfuss T, Linker R, Mäurer M, et al. Multiple Sclerosis Therapy Consensus Group (MSTCG): position statement on disease-modifying therapies for multiple sclerosis (white paper). Ther Adv Neurol Disord. 2021;14:175628642110396.
31. Macaron G, Larochelle C, Arbour N, Galmard M, Girard JM, Prat A, et al. Impact of aging on treatment considerations for multiple sclerosis patients. Front Neurol. 2023;14:1197212.
32. Constantinescu CS, Farooqi N, O'Brien K, Gran B. Experimental autoimmune encephalomyelitis (EAE) as a model for multiple sclerosis (MS). Br J Pharmacol. 2011;164:1079–106.
33. Buttigieg E, Scheller A, El Waly B, Kirchhoff F, Debarbieux F. Contribution of intravital neuroimaging to study animal models of multiple sclerosis. Neurotherapeutics. 2023;20:22–38.
34. Caravagna C, Jaouën A, Desplat-Jégo S, Fenrich KK, Bergot E, Luche H, et al. Diversity of innate immune cell subsets across spatial and temporal scales in an EAE mouse model. Sci Rep. 2018;8:5146.
35. Fenrich KK, Weber P, Hocine M, Zalc M, Rougon G, Debarbieux F. Long-term in vivo imaging of normal and pathological mouse spinal cord with subcellular resolution using implanted glass windows. J Physiol. 2012;590:3665–75.
36. Fenrich KK, Weber P, Rougon G, Debarbieux F. Implanting glass spinal cord windows in adult mice with experimental autoimmune encephalomyelitis. J Vis Exp. 2013;82:50826.
37. Mathis A, Mamidanna P, Cury KM, Abe T, Murthy VN, Mathis MW, et al. DeepLabCut: markerless pose estimation of user-defined body parts with deep learning. Nat Neurosci. 2018;21:1281–9.
38. Bhumbra GS, Beato M. Recurrent excitation between motoneurones propagates across segments and is purely glutamatergic. PLoS Biol. 2018;16: e2003586.
39. Harris-Warrick RM, Pecchi E, Drouillas B, Brocard F, Bos R. Effect of size on expression of bistability in mouse spinal motoneurons. J Neurophysiol. 2024;131:577–88.
40. Sekerli M, Del Negro CA, Lee RH, Butera RJ. Estimating action potential thresholds from neuronal time-series: new metrics and evaluation of methodologies. IEEE Trans Biomed Eng. 2004;51:1665–72.
41. Yousuf MS, Noh M-C, Friedman TN, Zubkow K, Johnson JC, Tenorio G, et al. Sensory neurons of the dorsal root ganglia become hyperexcitable in a T-cell-mediated MOG-EAE model of multiple sclerosis. eNeuro. 2019;6.
42. Sathyamurthy A, Johnson KR, Matson KJE, Dobrott CI, Li L, Ryba AR, et al. Massively parallel single nucleus transcriptional profiling defines spinal cord neurons and their activity during behavior. Cell Rep. 2018;22:2216–25.
43. Coull JAM, Beggs S, Boudreau D, Boivin D, Tsuda M, Inoue K, et al. BDNF from microglia causes the shift in neuronal anion gradient underlying neuropathic pain. Nature. 2005;438:1017–21.
44. Xu Q, Ford NC, He S, Huang Q, Anderson M, Chen Z, et al. Astrocytes contribute to pain gating in the spinal cord. Sci Adv. 2021;7:eabi6287.
45. Boulenguez P, Liabeuf S, Bos R, Bras H, Jean-Xavier C, Brocard C, et al. Down-regulation of the potassium-chloride cotransporter KCC2 contributes to spasticity after spinal cord injury. Nat Med. 2010;16:302–7.
46. Bos R, Sadlaoud K, Boulenguez P, Buttigieg D, Liabeuf S, Brocard C, et al. Activation of 5-HT2A receptors upregulates the function of the neuronal K-Cl cotransporter KCC2. Proc Natl Acad Sci USA. 2013;110:348–53.
47. Mazaud D, Capano A, Rouach N. The many ways astroglial connexins regulate neurotransmission and behavior. Glia. 2021;69:2527–45.
48. Barbay T, Pecchi E, Ducrocq M, Rouach N, Brocard F, Bos R. Astrocytic Kir4.1 channels regulate locomotion by orchestrating neuronal rhythmicity in the spinal network. Glia. 2023;71:1259–77.
49. Robel S, Sontheimer H. Glia as drivers of abnormal neuronal activity. Nat Neurosci. 2016;19:28–33.
50. Long D, Zhang Y, Liu A, Shen L, Wei H, Lou Q, et al. Microglia sustain anterior cingulate cortex neuronal hyperactivity in nicotine-induced pain. J Neuroinflammation. 2023;20:81.
51. Song B, Lee S-J, Kim C-H. Roles of cytokines in the temporal changes of microglial membrane currents and neuronal excitability and synaptic efficacy in ATP-induced cortical injury model. Int J Mol Sci. 2021;22:6853.
52. Datta Chaudhuri A, Dasgheyb RM, DeVine LR, Bi H, Cole RN, Haughey NJ. Stimulus-dependent modifications in astrocyte-derived extracellular vesicle cargo regulate neuronal excitability. Glia. 2020;68:128–44.
53. Escartin C, Galea E, Lakatos A, O'Callaghan JP, Petzold GC, Serrano-Pozo A, et al. Reactive astrocyte nomenclature, definitions, and future directions. Nat Neurosci. 2021;24:312–25.
54. Profaci CP, Munji RN, Pulido RS, Daneman R. The blood-brain barrier in health and disease: important unanswered questions. J Exp Med. 2020;217: e20190062.
55. Wu D, Chen Q, Chen X, Han F, Chen Z, Wang Y. The blood–brain barrier: structure, regulation, and drug delivery. Sig Transduct Target Ther. 2023;8:1–27.
56. Rua R, McGavern DB. Advances in meningeal immunity. Trends Mol Med. 2018;24:542–59.
57. Schnoor M, Alcaide P, Voisin M-B, van Buul JD. Crossing the vascular wall: common and unique mechanisms exploited by different leukocyte subsets during extravasation. Mediators Inflamm. 2015;2015: 946509.
58. Une H, Yamasaki R, Nagata S, Yamaguchi H, Nakamuta Y, Indiasari UC, et al. Brain gray matter astroglia-specific connexin 43 ablation attenuates spinal cord inflammatory demyelination. J Neuroinflammation. 2021;18:126.
59. Drake SS, Zaman A, Simas T, Fournier AE. Comparing RNA-sequencing datasets from astrocytes, oligodendrocytes, and microglia in multiple sclerosis identifies novel dysregulated genes relevant to inflammation and myelination. WIREs Mech Dis. 2023;15: e1594.
60. dos Santos AC, Barsante MM, Esteves Arantes RM, Bernard CCA, Teixeira MM, Carvalho-Tavares J. CCL2 and CCL5 mediate leukocyte adhesion in experimental autoimmune encephalomyelitis—an intravital microscopy study. J Neuroimmunol. 2005;162:122–9.
61. Lee H-G, Lee J-H, Flausino LE, Quintana FJ. Neuroinflammation: an astrocyte perspective. Sci Transl Med. 2023;15:eadi7828.
62. Wang X, Li X, Zuo X, Liang Z, Ding T, Li K, et al. Photobiomodulation inhibits the activation of neurotoxic microglia and astrocytes by inhibiting Lcn2/JAK2-STAT3 crosstalk after spinal cord injury in male rats. J Neuroinflammation. 2021;18:256.
63. Wang X, Zhang Z, Zhu Z, Liang Z, Zuo X, Ju C, et al. Photobiomodulation promotes repair following spinal cord injury by regulating the transformation of A1/A2 reactive astrocytes. Front Neurosci. 2021;15: 768262.
64. Sun J, Zhang J, Li K, Zheng Q, Song J, Liang Z, et al. Photobiomodulation therapy inhibit the activation and secretory of astrocytes by altering macrophage polarization. Cell Mol Neurobiol. 2020;40:141–52.
65. Huang Y-Y, Chen AC-H, Carroll JD, Hamblin MR. Biphasic dose response in low level light therapy. Dose Response. 2009;7:358–83.
66. Omi T, Kawana S, Sato S, Takezaki S, Honda M, Igarashi T, et al. Cutaneous immunological activation elicited by a low-fluence pulsed dye laser. Br J Dermatol. 2005;153(Suppl 2):57–62.
67. Weihrauch D, Keszler A, Lindemer B, Krolikowski J, Lohr NL. Red light stimulates vasodilation through extracellular vesicle trafficking. J Photochem Photobiol B. 2021;220: 112212.

68. Cao Y, Wu T, Yuan Z, Li D, Ni S, Hu J, et al. Three-dimensional imaging of microvasculature in the rat spinal cord following injury. Sci Rep. 2015;5:12643.
69. Salehpour F, Khademi M, Bragin DE, DiDuro JO. Photobiomodulation therapy and the glymphatic system: promising applications for augmenting the brain lymphatic drainage system. Int J Mol Sci. 2022;23:2975.
70. Abdelsalam M, Ahmed M, Osaid Z, Hamoudi R, Harati R. Insights into exosome transport through the blood–brain barrier and the potential therapeutical applications in brain diseases. Pharmaceuticals (Basel). 2023;16:571.
71. Emami Nejad A, Mostafavi Zadeh SM, Nickho H, Sadoogh Abbasian A, Forouzan A, Ahmadlou M, et al. The role of microRNAs involved in the disorder of blood–brain barrier in the pathogenesis of multiple sclerosis. Front Immunol. 2023. https://doi.org/10.3389/fimmu.2023.1281567.
72. Martin CR, Osadchiy V, Kalani A, Mayer EA. The brain–gut–microbiome axis. Cell Mol Gastroenterol Hepatol. 2018;6:133–48.
73. Agirman G, Yu KB, Hsiao EY. Signaling inflammation across the gut–brain axis. Science. 2021;374:1087–92.
74. Rojas OL, Pröbstel A-K, Porfilio EA, Wang AA, Charabati M, Sun T, et al. Recirculating intestinal IgA-producing cells regulate neuroinflammation via IL-10. Cell. 2019;176:610-624.e18.
75. Johanson DM, Goertz JE, Marin IA, Costello J, Overall CC, Gaultier A. Experimental autoimmune encephalomyelitis is associated with changes of the microbiota composition in the gastrointestinal tract. Sci Rep. 2020;10:15183.
76. Kadowaki A, Quintana FJ. The gut–CNS axis in multiple sclerosis. Trends Neurosci. 2020;43:622–34.
77. Zilionis R, Engblom C, Pfirschke C, Savova V, Zemmour D, Saatcioglu HD, et al. Single-cell transcriptomics of human and mouse lung cancers reveals conserved myeloid populations across individuals and species. Immunity. 2019;50:1317-1334.e10.

Publisher's Note